

First Direct Observational Evidence for Secondary Gravity Waves Generated by Mountain Waves over the Andes

Masaru Kogure¹, Jia Yue², Takuji Nakamura³, Lars Hoffmann⁴, Sharon L. Vadas⁵, Yoshihiro Tomikawa³, Mitsumu K. Ejiri³, and Diego Janches⁶

¹Kyushu University

²Goddard Space Flight Center

³National Institute of Polar Research

⁴Forschungszentrum Jülich

⁵NorthWest Research Associates, Inc.

⁶National Aeronautics and Space Administration (NASA)

November 22, 2022

Abstract

A mountain wave with a significant brightness temperature amplitude and ~ 500 km horizontal wavelength was observed over the Southern Andes on 24–25 July 2017 in AIRS/Aqua satellite data. In the MERRA-2 reanalysis data, a mesoscale vortex-like pattern appeared to the west of the Andes at 2 km, and the wind flowed over the Andes. VIIRS/Suomi-NPP did not detect the mountain waves; however, it observed concentric ring-like waves in the nightglow emissions at ~ 87 km with ~ 100 km wavelengths on the same night over and leeward of the Southern Andes. A ray tracing analysis showed that the mountain waves propagated to the east of the Andes, where concentric ring-like waves appeared while mountain waves broke. Therefore, the concentric ring-like waves were likely secondary gravity waves generated by momentum deposition that accompanied mountain wave breaking. These results provide the first direct evidence for secondary gravity waves generated by momentum deposition.

First Direct Observational Evidence for Secondary Gravity Waves Generated by Mountain Waves over the Andes

Masaru Kogure¹, Jia Yue^{2,3}, Takuji Nakamura^{4,5}, Lars Hoffmann⁶, Sharon L. Vadas⁷, Yoshihiro Tomikawa^{4,5}, Mitsumu K. Ejiri^{4,5}, Diego Janches^{2,3}

¹Department of Earth and Planetary Science, Kyushu University, 744 Motooka Nishi-ku, Fukuoka, Japan

²NASA Goddard Space Flight Center, 8800 Greenbelt Rd, Greenbelt, MD, USA

³Catholic University of America, 620 Michigan Ave NE, Washington, DC, USA

⁴National Institute of Polar Research, 10-3, Midori-cho, Tachikawa-shi, Tokyo, Japan

⁵The Graduate University for Advanced Studies, SOKENDAI, 10-3, Midori-cho, Tachikawa-shi, Tokyo, Japan

⁶Forschungszentrum Jülich, Wilhelm-Johnen-Straße, 52428 Jülich, Germany

⁷NorthWest Research Associates, 3380 Mitchell Lane, Boulder, CO, USA

Corresponding author: Masaru Kogure (kogure.masaru.695@m.kyushu-u.ac.jp)

Key Points:

- VIIRS captured nightglow concentric ring-like gravity waves in mesopause east of Southern Andes during intense winter mountain wave event.
- Mountain waves observed by AIRS likely broke while the waves were propagating upward and eastward.
- Concentric ring-like gravity waves captured by VIIRS were likely generated by a local body force created by mountain wave breaking.

Abstract

A mountain wave with a significant brightness temperature amplitude and ~500 km horizontal wavelength was observed over the Southern Andes on 24–25 July 2017 in AIRS/Aqua satellite data. In the MERRA-2 reanalysis data, a mesoscale vortex-like pattern appeared to the west of the Andes at 2 km, and the wind flowed over the Andes. VIIRS/Suomi-NPP did not detect the mountain waves; however, it observed concentric ring-like waves in the nightglow emissions at ~87 km with ~100 km wavelengths on the same night over and leeward of the Southern Andes. A ray tracing analysis showed that the mountain waves propagated to the east of the Andes, where concentric ring-like waves appeared while mountain waves broke. Therefore, the concentric ring-like waves were likely secondary gravity waves generated by momentum deposition that accompanied mountain wave breaking. These results provide the first direct evidence for secondary gravity waves generated by momentum deposition.

Plain Language Summary

A recent model study (Vadas and Becker, 2019) showed that mountain waves created over the Andes broke in the stratosphere and mesosphere, thereby depositing their momentum and creating “secondary” gravity waves. These secondary waves then propagated into the lower thermosphere and created high-order waves, some of which propagated to the upper thermosphere. This vertical multistep coupling mechanism is likely important for creating ionospheric disturbances in the F region. However, observational evidence supporting this mechanism is lacking. The purpose of this study is to show observational evidence using data from two satellite instruments: AIRS/Aqua and VIIRS/Suomi-NPP. AIRS captured a mountain wave with a significant amplitude in the stratosphere over the Andes on 24–25 July 2017. VIIRS/Suomi-NPP did not detect the mountain waves but instead observed concentric ring-like gravity waves in the upper mesosphere on the leeward of the Andes. The concentric ring-like structure is one of the features of secondary waves created from momentum deposition that accompanies breaking gravity waves; thus, we conclude that the observed gravity waves were likely secondary gravity waves. These observational results provide the first direct evidence for secondary gravity waves generated by momentum deposition from breaking mountain waves and support the vertical multistep coupling mechanism.

Keywords: Middle atmosphere, Secondary gravity wave, AIRS/Aqua, VIIR/Suomi-NPP, Andes, Mountain wave

1 Introduction

Gravity waves (GWs) play an important role in driving atmospheric circulation, which affects the temperature structure and distribution of chemical components (*Fritts and Alexander, 2003; Butchart et al., 2010*). Mountain waves are one type of GW and are emitted from wind flowing over a topography. Mountain waves transport a significant amount of momentum from the lower to the middle atmosphere, a process that is typically parameterized in numerical models (*Fritts and Alexander, 2003; Alexander et al., 2010; Butchart et al., 2010*). Mountain waves have been studied using various observations, theoretical considerations, and numerical simulations over the last few decades. Satellite observational instruments such as the atmospheric infrared sounder (AIRS) (*Hoffmann et al., 2013; Ern et al., 2017*), microwave limb sounder (MLS) (*Wu and Eckermann, 2008*), and sounding of the atmosphere using broadband emission radiometry (SABER) (*Preusse et al., 2009*) have provided global maps of GW

activity. They have shown that the Andes are one of the most intense GW activity regions in the middle atmosphere due to mountain waves caused by wind flowing over the Andes. The high GW activity region extends leeward (or eastward) of the Andes due to the polar night jet (*Sato et al.*, 2012).

Mountain waves theoretically have quasi-stationary ground-based phase velocity and may encounter a critical level in weak wind layers (*Fritts and Alexander*, 2003). When GWs break, they not only accelerate background circulation but also excite secondary GWs (*Vadas et al.*, 2003; *Bacmeister and Schoeberl*, 1989; *Heale et al.*, 2020). A few observational studies have shown statistically that secondary GWs are likely associated with mountain wave events over the Andes. *de Wit et al.* (2017) estimated GW momentum flux over the Southern Andes using meteor radar wind measurements and found a significant vertical flux of eastward momentum in the mesosphere and lower thermosphere. GW sources in the troposphere cannot explain this eastward momentum flux because a polar vortex is present over the Southern Andes. *de Wit et al.* (2017) argued that secondary GWs contributed to this eastward momentum flux. *Liu et al.* (2019) found high mountain wave activity in the Austral winter over the Andes up to altitudes of 55 km that attenuated between 55-65 km of altitude. GW activity increased again above 65 km of altitude with a westward tilt. Their results suggest that breaking mountain waves over the Andes generate secondary GWs. However, to the best of our knowledge, no direct nadir simultaneous observations of a mountain wave and the corresponding secondary wave have been reported.

Two mechanisms can generate secondary GWs: nonlinear fluid interactions and local body forces (*Vadas and Becker*, 2018; *Heale et al.*, 2020). Nonlinear interactions result in a cascade of energy to smaller-scales and the generation of secondary GWs that have smaller scales than those of the primary GWs (*Fritts et al.*, 1994; *Andreassen et al.*, 1998; *Fritts et al.*, 1998). *Bossert et al.* (2015) observed small-scale GWs in a warm phase front of a mountain wave over Mount Cook, New Zealand by using Advanced Mesosphere Temperature Mapper observations aboard an aircraft. *Heale et al.* (2017) simulated this event by using a 2-D nonlinear model and found that secondary GWs were created in the warm phase where instabilities were excited due to primary GWs breaking. The secondary GWs had smaller horizontal wavelengths than the wavelength of the mountain wave by one order of magnitude and had broad phase velocity spectra.

Alternatively, secondary GWs can also be created by local body forces such as temporally and spatially localized wave drag, created by the deposition of momentum that accompanies primary GW breaking. A local body force creates an imbalance in the flow so that the resultant wave-mean flow interaction generates secondary GWs (*Vadas et al.*, 2003, 2018). The latter secondary GW spectra have broad horizontal phase speeds, periods, and wavelengths, and propagate in all azimuths except perpendicular to the body force direction. These spectra depend on the size and duration of the local body force. Some secondary GWs can avoid breaking or reaching critical levels over large distances and thus can "carry" momentum and energy into the upper atmosphere. *Vadas et al.* (2003, 2018) simulated secondary GWs created by a local body force using a Fourier-Laplace model. They found that the peaks of the horizontal and vertical wavelength spectra were ~2 times larger than the horizontal and 1-2 times larger than the vertical sizes of the local body force. In addition, the peak of the period spectrum was the characteristic period of the body force unless the duration was longer.

Vadas and Becker (2019) showed that during a strong mountain wave event, the mountain waves break near the stratopause, thereby generating secondary GWs from local body

forces. These secondary GWs then propagated higher, where they broke and dissipated at an altitude between ~80-130 km, thereby creating tertiary GWs that propagated higher into the thermosphere. Such higher-order GWs were likely observed by the GOCE satellite (*Vadas et al., 2019*) as “hotspot” traveling atmospheric disturbances, (*Trinh et al., 2018*), which was verified by a recent modeling study (*Becker and Vadas, JGR, submitted*). Thus, this strongly suggests that momentum and energy are transported into the upper thermosphere via a vertical multistep coupling mechanism (see Figure 21 in *Vadas and Becker, 2019*).

Using a high-resolution model, *Vadas et al. (2018)* demonstrated that secondary GWs have “fishbone structures” in vertical time slices, which indicates that secondary GWs radiate up and down from primary GW breaking regions. They also found several fishbone structures near the winter stratopause over McMurdo in lidar data. Secondary GWs from mountain wave breaking over the Andes were simulated using a high-resolution, GW-resolving general circulation model (*Becker and Vadas, 2018*). *Vadas and Becker (2019)* showed that secondary GWs had concentric ring-like structures. A concentric ring-like GW was captured over Chile in OH imager data, and no convection appeared near the OH imager site (*Vargas et al., 2016*). They inferred that the ring-like GW was generated by a primary GW breaking (possibly generated by convection over Bolivia), although they did not capture the primary GW.

The purpose of this study is to provide the first direct observational evidence that ring-like secondary GWs in the mesopause are created from mountain waves over the Andes, similar to *Vadas and Becker (2019)*. According to their model results, the strong eastward wind flowing over the Andes creates mountain waves with large amplitudes, and the mountain waves propagate upward and break at 50-80 km altitude. The momentum deposition that accompanies this breaking process generates local body forces that excite secondary GWs with partial concentric ring-like structures. Some of these secondary GWs then propagate to 100 km. Observations from two satellite instruments, AIRS and the Visible/Infrared Imaging Radiometer Suite (VIIRS), were used to capture both mountain waves and secondary GWs. AIRS can observe GWs at an altitude range of approximately 20-50 km and observed mountain waves during this event. VIIRS observes OH airglow intensity and captured secondary GWs with ring-like structures at an altitude of ~87 km during this event.

2 Satellite observations of gravity waves: AIRS and VIIRS

2.1 Atmospheric Infrared Sounder (AIRS)

The AIRS instrument aboard the NASA Aqua satellite (*Aumann et al., 2003; Chahine et al., 2006*) measures infrared radiance spectra in three spectral bands between 3.74 and 15.4 μm . The Aqua satellite was launched in 2002. Aqua has an orbit altitude of 705 km and an orbit period of ~100 min, with local equatorial crossing times of ~1:30 PM and 1:30 AM. AIRS uses cross-track scanning, with each scan consisting of 90 footprints over 1,780 km of ground distance and a separation of 18 km of along-track distance. The footprint size varies between $14 \times 14 \text{ km}^2$ at nadir and $21 \times 42 \text{ km}^2$ at the edges of the scan. AIRS measurements in the 4.3 and 15 μm CO_2 bands have been applied in various studies of stratospheric GWs. Here, 15 μm brightness temperature data averaged over two sets of AIRS channels were used to investigate mountain waves in the stratosphere. First, the brightness temperatures observed in multiple AIRS channels were averaged to reduce the measurement noise. Two channel sets were used for averaging, with temperature kernel functions peaking in two layers around ~23 and ~40 km of altitude. The weighing functions have typical full widths at half maximum of ~15 km and

therefore represent mean temperatures over the altitude ranges of 17–32 and 34–49 km, respectively. Second, a fourth-order polynomial fit was subtracted for each across-track scan to remove the background temperatures. The remaining brightness temperature perturbations provide a measure of GWs with vertical wavelengths longer than 10–15 km and horizontal wavelengths longer than 30–80 km. The AIRS/Aqua observations of GWs are described in more detail by *Hoffmann et al.* (2013, 2017).

2.2 Visible/Infrared Imaging Radiometer Suite (VIIRS)

The VIIRS instrument aboard the NOAA/NASA Suomi-NPP satellite, launched in 2011, provides global coverage of visible and infrared wavelength spectra (*Miller et al.*, 2015). Its orbit period and local equatorial crossing times are almost the same as Aqua's, but its orbit altitude is 834 km. VIIRS has 22 channels ranging between 0.41 and 12.01 μm . The day/night band (DNB) sensor is one of the channels and can detect very faint light within 0.505–0.89 μm ; therefore, the DNB sensor can capture OH airglow intensity modulated by GWs at an altitude of ~ 87 km. The horizontal spatial resolution and coverage of the DNB sensor is high ($0.74 \times 0.74 \text{ km}^2$ and a 3,000 km across-track swath width) and is preserved across the entire swath. Thus, the DNB sensor can capture very small GWs with a horizontal wavelength of several kilometers. In terms of the minimum vertical wavelength (λ_z) of GWs, the ability of the DNB to detect OH airglow intensity modulation depends on the OH airglow thickness so the DNB can typically detect GWs with $\lambda_z \geq 10$ km.

However, DNB also captures reflections from clouds. Tropospheric clouds frequently have wave structures, which makes it difficult to distinguish them from GW modulations in the OH airglow layer. The M15 band sensor is one of the 22 channels in VIIRS and can detect cloud infrared brightness signals (9.8–11.8 μm). This sensor enables us to distinguish GW modulation in the OH airglow layer from cloud reflections.

3 AIRS and VIIRS observations of primary and secondary GWs

3.1. GWs with strong amplitudes captured by AIRS on 24–25 July 2017

AIRS captured mountain waves with strong amplitudes over the Southern Andes on 24 July 2017, 18:32–18:42 UT and 25 July 2017, 05:43–05:53 UT. Figures 1 (a) and (b) show brightness temperature perturbations at altitudes of ~ 23 and ~ 40 km on 24 July, respectively. Figures 1 (c) and (d) show the perturbations at the same altitudes on 25 July. The GWs were present directly above the Andes in both layers at both observation times, although the GWs on 25 July were further southward. The GW wavefronts were almost parallel to the Andes mountain chain, which extends from 10°N to 55°S on the west side of the South American continent. Figures 1 (e) and (f) show the horizontal wind at 2 km altitude at 12 UT on 24 July and at 0 UT on 25 July, respectively. A mesoscale vortex-like pattern appears upwind of the Andes, and its center is located around 100°W , 57°S at 12 UT on 24 July. Eastward tropospheric winds over the Andes are strong (~ 20 – 40 m s^{-1}) in the northeast side of the vortex-like pattern. Such wind conditions in the lower troposphere are favorable for the occurrence of a strong mountain wave event (*Vadas and Becker*, 2019). A backward GW ray tracing simulation was performed with the same model, initial GWs parameters, and background meteorological conditions in Section 4. The ray tracing result showed that the observed GW originated from the Andes, which suggests that the GWs were mountain waves. The strong wind region over the Andes moved southward at 0 UT on 25 July, and the observed GWs also moved southward on 25 July in conjunction with the

strong wind (Figure 1 (f)). Thus, the observed GWs lasted at least ~11 h and were most likely mountain waves.

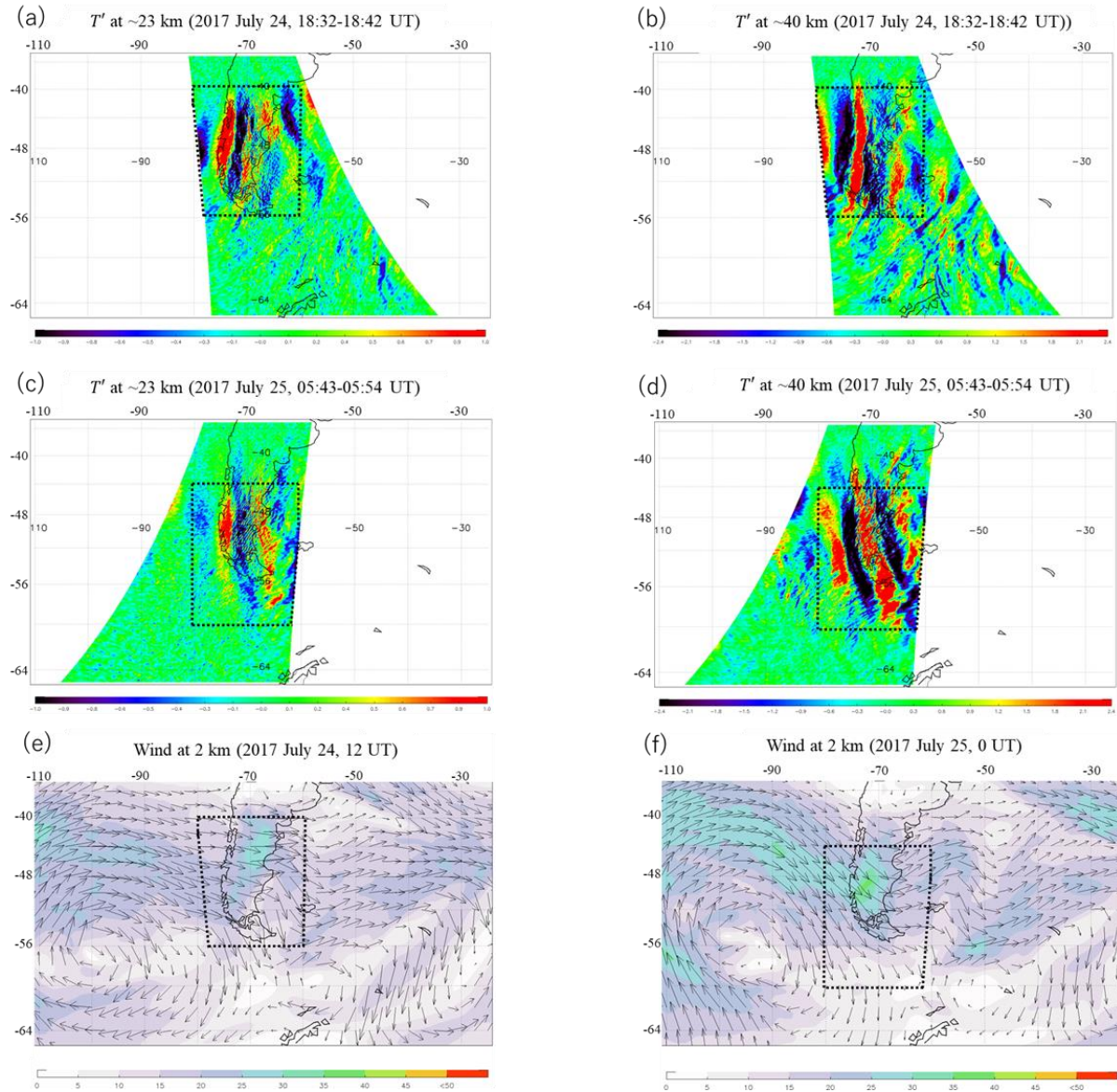


Figure 1. (a) and (b) show 15 μ m brightness temperature perturbations from AIRS with GWs at altitudes of ~23 and ~40 km at 18:32-18:42 UT on 24 July 2017, respectively. (c) and (d) show the same as a and b, but at 05:43-05:54 on 25 July 2017. (e) and (f) show the MERRA-2 low-level winds at an altitude of 2 km at 12 UT on 24 July and 0 UT on 25 July, respectively.

3.2. Concentric ring-like waves captured by VIIRS

Suomi-NPP passed over the Andes between 04:15-04:26 UT on 25 July 2017. Before this time, mountain waves were present for many hours (Figure 1). Figure 2 (a) shows the OH airglow perturbations where waves are present at 30—70°W, 48—64°S. Their wavelengths are approximately 100 km so the bandpass Butterworth filter with a cutoff at 50—220 km was applied to the OH intensity deviations to retrieve the wave structures (Figure 2 (b)). Many waves

overlap the leeward side of the Andes. The red dashed lines in Figure 2 (b) indicate some of these waves. Most are curved structures. Figure 2 (c) shows the brightness temperatures from the M15 channel at the same time as Figure 2 (a) and (b). Some wave-like cloud structures can be seen in Figure 2 (c). The red dashed lines in Figure 2 (c) indicate examples of wave-like cloud structures. The same structures are present in the OH intensity in Figure 2 (a) and (b) and are therefore not created by GWs, but rather by reflections of clouds. However, the fine wave structures extending leeward are not found in Figure 2 (c) and are therefore structures created by GWs (i.e., the wavefronts indicated by the red dashed lines in Figure 2 (b)).

To the best of our knowledge, GWs with concentric ring-like structures can be created from two mechanisms: secondary generation from temporally and spatially localized momentum deposition (*Vadas et al.*, 2003, 2019) and deep convection (*Taylor and Hapgood*, 1988). One of the main features of both mechanisms is a curved front, i.e., a partial concentric ring, which appears in Figure 2(b). This allows the apparent centers of the concentric ring structure to be determined. A concentric ring structure is distorted and moves leeward from the actual epicenter of a wave and has been shown to occur when concentric GWs propagate in a strong wind (*Vadas et al.*, 2009), and likely occurs here from the polar night jet. In the case of *Vadas et al.* (2009), concentric GWs were created by deep convection. However, deep convection is unlikely to occur at $\sim 50^\circ\text{S}$ during July, which is wintertime in the southern hemisphere, and there was no deep convection in Figure 2 (c). In addition, a transmission diagram was calculated from MERRA-2 data in accordance with *Tomikwa* (2015) and shows that GWs with 80–120 km wavelengths and east-to-south phase velocities hardly penetrated the stratosphere from the tropopause (not shown) around the Southern Andes. Thus, the concentric ring-like GWs observed here are likely not convective GWs. These ring-like GWs are probably secondary GWs generated by local body forces created from mountain waves breaking in the stratosphere and the mesosphere, as discussed in the next section.

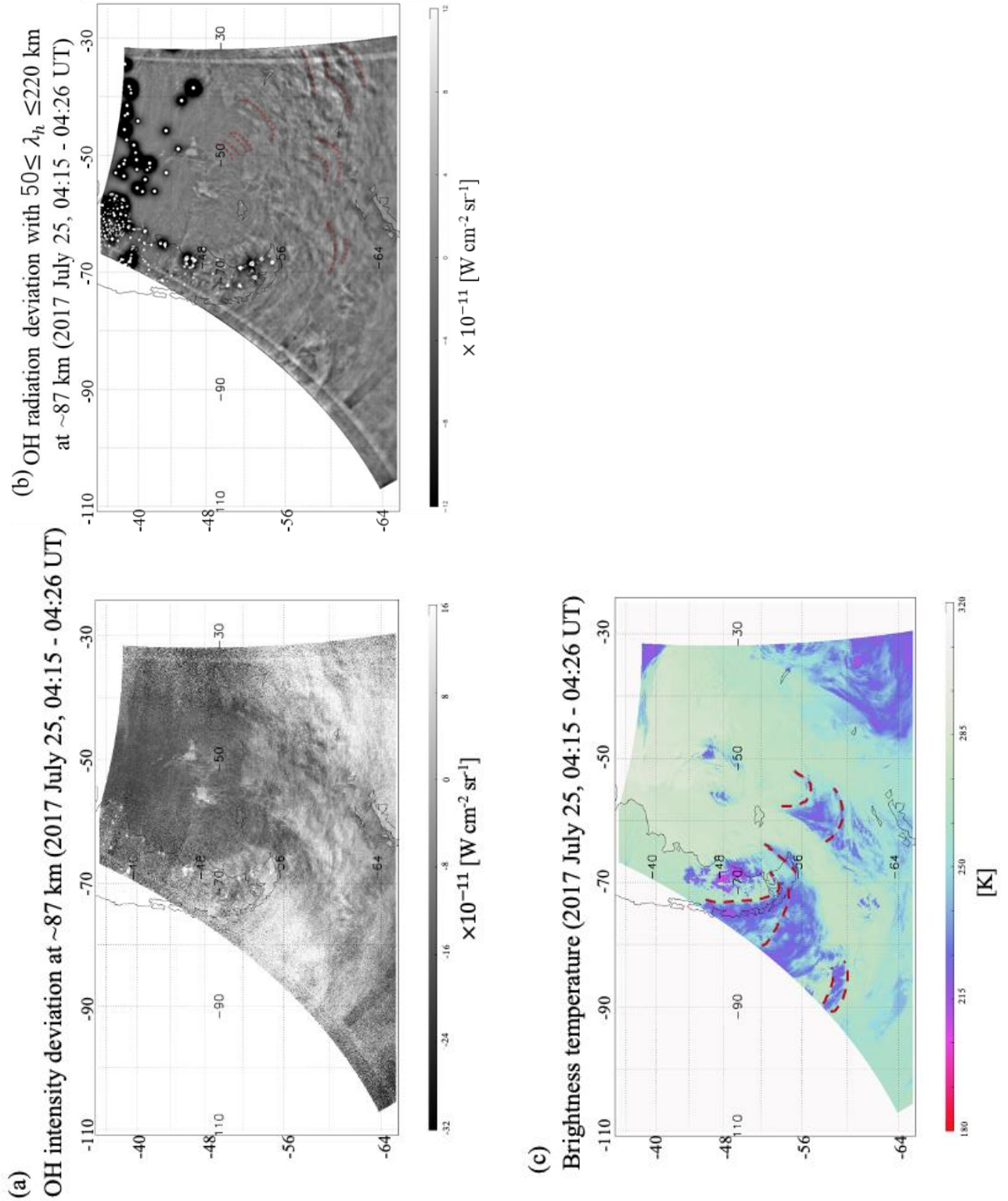


Figure 2. (a) OH intensity deviation at an altitude of ~87 km at 04:15-04:26 on 25 July 2017. (b) The same as in (a), but the deviations have been filtered with a bandpass filter allowing for wavelengths in the range of 50-220 km. (c) Brightness temperatures of clouds at the same time at 9.8-11.8 μm .

4 Mountain Waves Breaking

In our case study, the AIRS observations show mountain waves, and the VIIRS observations show concentric ring-like waves with multiple apparent centers leeward of the Andes (Figure 2 (b)). These features suggest that mountain waves propagate and break in the stratosphere or lower mesosphere, where they create local body forces. *Sato et al.* (2012) pointed out that MWs over the Andes preferentially propagate leeward due to refraction caused by wind shear of the polar night jet. Using a high-resolution GW-resolving global circulation model, *Vadas and Becker* (2019) demonstrated that local body forces caused by MWs breaking over the Andes extended leeward and southward at an altitude range of 50-80 km (Figures 8 and 9 in *Vadas and Becker* (2019)). *Vadas and Becker* (2019) also showed that these forces were located at the center of concentric ring-like GWs, which suggests that the concentric ring-like GWs are secondary GWs. Each body force excites secondary GWs with concentric ring-like structures, as shown in *Vadas et al.* (2018). The MWs over the Andes tend to break in the stratosphere or lower mesosphere at and above the altitude where the polar night is at a maximum during winter due to convective instability or critical level filtering (*Vadas and Becker*, 2019). However, weak-amplitude mountain waves can also propagate into the OH layer if no wind reversals occur (*Smith et al.*, 2009; *Bossert et al.*, 2015). Here, the VIIRS observations showed that stationary mountain waves were not present near the mesopause.

To estimate the paths of the mountain waves and their breaking/saturation locations or local body force locations, a forward GW ray tracing simulation was performed. Our ray tracing model is the same as that of *Kogure et al.* (2018), and its mathematical theory is based on *Marks and Eckerman* (1995) and *Dunkerton* (1984). The background wind and temperature were obtained from the MERRA-2 reanalysis. It should be noted that the MERRA-2 data between 0.1 and 0.01 hPa (altitude of ~68-75 km) are uncertain due to the upper boundary condition (*Gelaro et al.*, 2017). The background fields were defined as mean values from 18 UT on 24 July to 06 UT on 25 July, the period during which the mountain waves were observed. The ground-based initial period of the mountain waves was assumed to be 0 s because the mountain waves are approximately stationary (*Dunkerton*, 1984), and the sign of their vertical group velocity is upward. The initial altitude for the mountain waves was assumed to be 40 km, which is the most sensitive altitude of the weighting functions for the AIRS brightness temperature observations. The initial horizontal wave vectors were derived from AIRS brightness temperature perturbations. The perturbations in the dashed frame in Figure 2 (b) were analyzed using the Lomb–Scargle method (*Scargle* 1982) to derive a 2D Lomb–Scargle periodogram. The wavenumber at the maximum power is $1.2 \times 10^{-2} \text{ km}^{-1}$, which corresponds to a wavelength of ~520 km and was used as the initial value. The azimuthal angles of the wave vectors at the power maximum are 86° and 266° clockwise from north. It should be noted that the azimuthal angle has an 180° ambiguity due to the 2D spectral analysis. However, the propagation direction of a mountain wave is opposite to the background wind over a surface obstacle (*Nappo*, 2002). The eastward wind at 2 km altitude over the Andes mountain chain (Figure 2 (e, f)) is eastward; thus, 266° was chosen for the initial azimuthal angle. Gravity wave ray tracing was conducted at 9 points ($70^\circ \pm 8^\circ \text{W}$, $48^\circ \pm 8^\circ \text{S}$).

GWs break when they reach critical levels or when they become unstable. These instabilities are classified into two types: shear instability and convective instability. Our ray tracing analysis can estimate the locations for critical levels of mountain waves, but cannot

identify locations of instabilities caused by mountain waves. To investigate the occurrence of the instabilities of the mountain waves, the Richardson number, R_i , and the ratio between the horizontal wind amplitude (u'_{amp}) and the intrinsic horizontal phase speed (c) were estimated along the ray path of each mountain wave. When R_i is less than 0.25, this indicates the likelihood of shear instability (Fritts and Alexander, 2003). Convective instability is possible when the ratio u'_{amp}/c is larger than 0.7-1 (Vadas and Becker, 2019). In accordance with Vadas and Becker (2019), the threshold for the ratio was 0.7. The temperature amplitude, T'_{amp} , at the initial altitude (40 km altitude) were derived from the variance of the brightness temperature in the dashed frame in Figure 2 (b). In this case, T'_{amp} is 3 K. u'_{amp} was estimated with the assumption of initial GW by equation (10) in Geller and Gong (2010). The T'_{amp} and u'_{amp} values at the altitude of the next step was calculated from the total GW energy, assuming that the energy increases with an e-folding at twice the density scale height (Alexander et al., 2011; Kogure et al., 2017; Liu et al., 2014; Lu et al., 2015).

Figure 3 shows the ray paths of the mountain waves superimposed on Figure 2 (b). Triangles indicate where the waves may have encountered shear instability. Almost all waves encountered critical levels at altitudes of ~60 km, except for two waves that originated at 70°W, 56°S and 62°W, 56°S. These two waves reached the model top (~75 km) of MERRA-2. All waves had a preference to propagate leeward. Moreover, all waves began to meet the shear instability condition at altitudes of ~60 km. Most waves began to meet the convective instability condition a few kilometers higher in altitude than those of the shear instability condition. However, one wave that originated at 62°W, 56°S met the convective instability condition at ~10 km higher altitude (~72 km) and two waves originating at 70°W, 56°S and 77°W, 56°S did not meet the condition (not shown). Since brightness temperature variances observed by AIRS are typically much smaller than the actual atmospheric temperature variance (Hoffmann et al., 2014), these waves possibly met the conditions at lower altitudes than those in our ray tracing results. These results indicate that the mountain waves propagated to the region where the concentric ring-like GWs appeared, and then they broke. This result is consistent with the model study of Vadas and Becker (2019).

It should be noted that the centers of some concentric ring-like GWs (around 35°E, 60°S) are far (~1000 km) from the edge of the ray tracing results (55°E, 56°S). This horizontal distance could be explained by two possibilities. One possibility is that background horizontal wind above the observable altitude of AIRS accelerated rapidly in the eastward direction in time. This would cause the MWs to be swept thousands of kilometers downstream before breaking (Vadas and Becker, 2018). Such acceleration would not be captured by the MERRA-2 winds. Another possibility is that some mountain waves were present further leeward in the stratosphere than the waves captured by AIRS. A mountain wave with a larger perpendicular component to the zonal wind of its wave vector over the Andes has a preference to propagate leeward (Sato et al., 2012). Such a mountain wave should have a small vertical wavelength because the vertical wavelength of a mountain wave is proportional to a parallel component of a background wind (Nappo, 2002). Since AIRS cannot detect GWs with vertical wavelengths less than ~12 km, it is possible that AIRS failed to detect these mountain waves in the leeward direction, although the mountain waves broke and created the concentric ring-like waves seen by VIIRS.

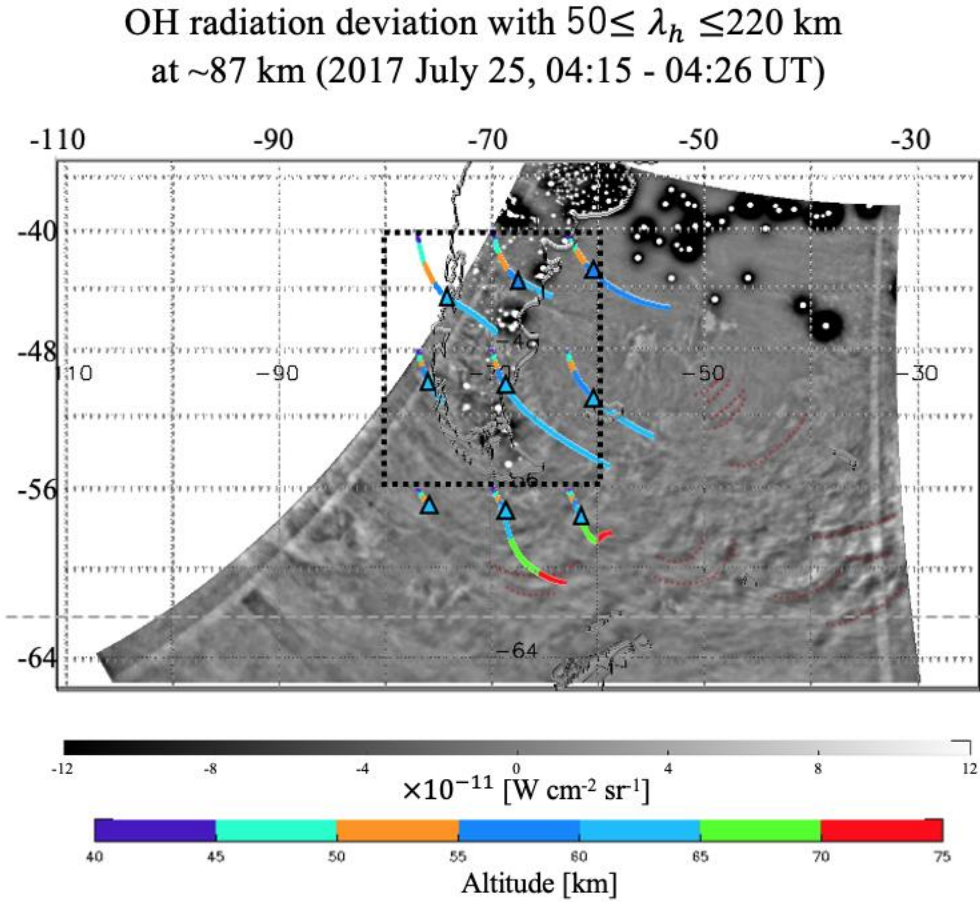


Figure 3. The ray tracing results are superimposed on Figure 2b. The colors indicate the altitude of each mountain wave. The triangles indicate the estimated locations of shear instability.

Thus, we conclude that the concentric ring-like GWs observed here were likely secondary GWs caused by local body forces from breaking mountain waves. These results are the first direct observational evidence for a similar phenomenon simulated by *Vadas and Becker* (2019) where mountain waves over the Andes create secondary GWs with a concentric ring-like structure. However, the horizontal wavelengths of the observed secondary GWs (~ 100 km) were much shorter than those in their model (500-2000 km). The inconsistency between the observations and the model could be due to the fact that the minimum horizontal wavelength resolvable by *Vadas and Becker* (2019) was ~ 165 km (i.e., the model had a horizontal grid spacing of ~ 65 km). This implies that their model cannot simulate the small-scale concentric GWs observed by VIIRS. Additionally, GWs are only observable in the OH layer if they have vertical wavelengths > 10 km (*Liu and Swenson*, 2003). Since the secondary GW spectrum excited by a local body force is quite broad (*Vadas et al.*, 2003) and many of the large-scale secondary GWs observed in *Vadas and Becker* (2019) have smaller vertical wavelengths, it is possible that they were not seen in the OH airglow layer. Finally, although VIIRS can potentially capture GWs with ~ 1000 km horizontal wavelengths because of its wide field of view, portions of the VIIRS images are frequently contaminated with clouds or city lights, making it difficult to

capture large-scale GWs. Thus, VIIRS tends to be sensitive to secondary GWs with smaller horizontal wavelengths than those in the *Vadas and Becker* (2019) model.

5 Conclusion

AIRS captured a mountain wave event with significant brightness temperature amplitudes (3 K) in the stratosphere and ~500 km horizontal wavelengths over the Southern Andes on 24–25 July 2017. During this event, VIIRS did not detect mountain waves but instead observed concentric ring-like GWs with ~100 km wavelengths at 04:30 UT on the same night leeward of the Southern Andes. Our ray tracing result shows that the mountain waves propagated to the east where the concentric GWs appeared while the mountain waves were breaking. Thus, the concentric waves were probably secondary GWs generated by local body forces created by the breaking mountain waves. These observational results are consistent with the model results of *Vadas and Becker* (2019), except for the horizontal wavelengths of the secondary GWs. This difference in horizontal wavelengths could be due to differing coverage of the GW spectrum between the VIIRS observations and the model. This study shows the first concrete evidence that secondary GWs are generated by mountain waves over the Andes and have concentric or ring-like structures. In addition, this study supports the theory of *Vadas and Becker* (2019) for vertical coupling via secondary and higher-order GWs throughout the middle and upper atmosphere.

Acknowledgments, Samples, and Data

This study was supported by JSPS KAKENHI 19K23465 and the Scientific Committee on Antarctic Research (SCAR) fellowship award 2019. SLV was supported by NSF grant AGS-1832988 and by NASA grant 80NSSC19K0836. J. Y. was supported by NSF grants AGS-1651394 and AGS-1834222, and by NASA grant 80NSSC19K0836.

VIIRS DNB and M15 data are distributed by the Comprehensive Large Array-data Stewardship System (CLASS) from the National Oceanic and Atmosphere (<https://www.avl.class.noaa.gov/saa/products/welcome;jsessionid=F8A8750F39D62D7C82672D9640A3D532>). MERRA-2 data were obtained at <http://disc.sci.gsfc.nasa.gov>. The AIRS/Aqua gravity wave datasets (Hoffmann et al., 2017) are provided by Forschungszentrum Jülich (https://datapub.fz-juelich.de/slcs/airs/gravity_waves/data).

References

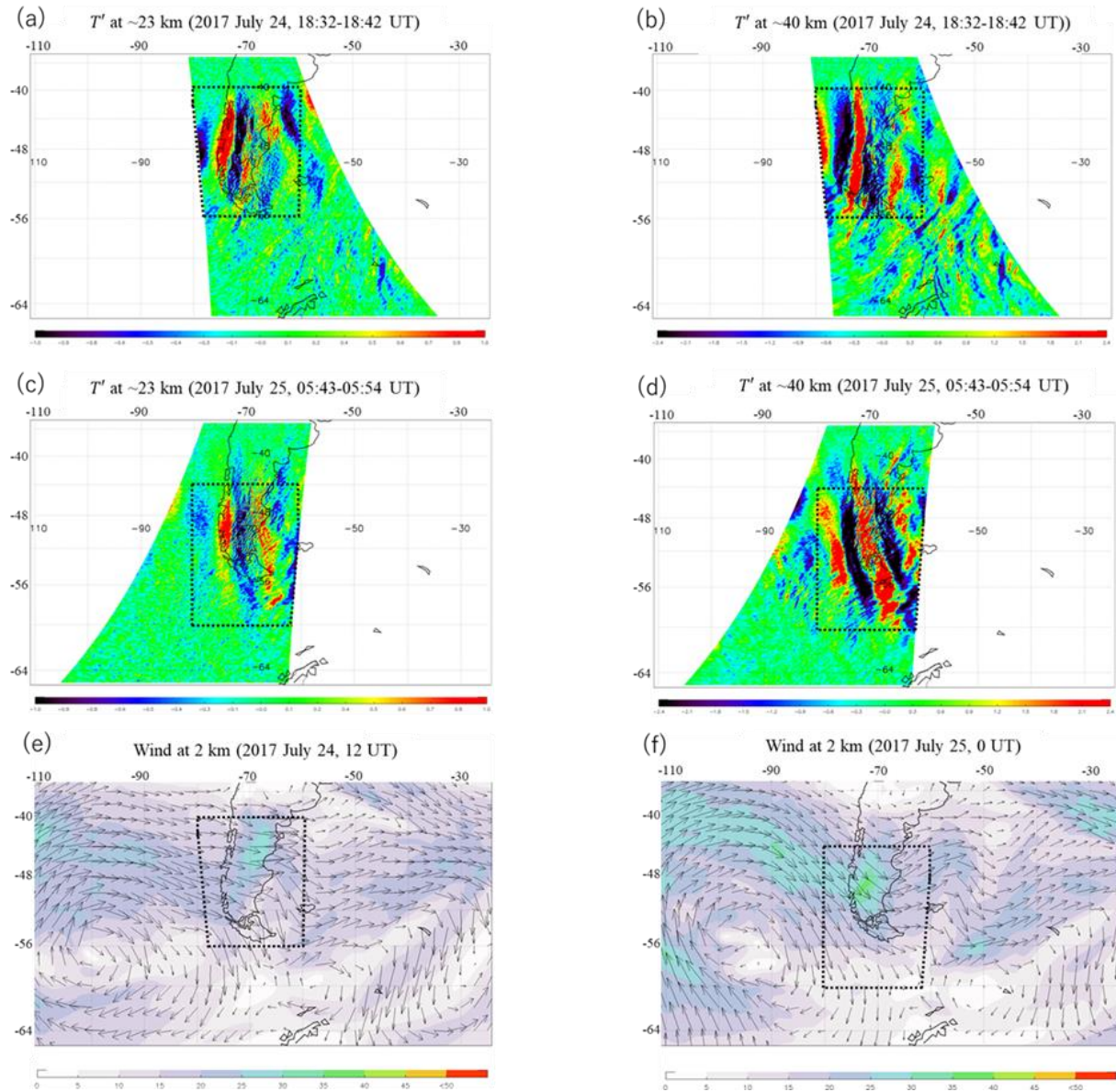
- Alexander, M.J., Geller, M., McLandress, C., Polavarapu, S., Preusse, P., Sassi, F., et al. (2010). Recent developments in gravity-wave effects in climate models and the global distribution of gravity-wave momentum flux from observations and models. *Quarterly Journal of the Royal Meteorological Society*, 136: 1103–1124. doi:10.1002/qj.637
- Alexander, S. P., Klekociuk, A. R., & Murphy, D. J. (2011). Rayleigh lidar observations of gravity wave activity in the winter upper stratosphere and lower mesosphere above Davis, Antarctica (69°S, 78°E). *Journal of Geophysical Research*, 116, D13109. doi:10.1029/2010JD015164
- Andreassen, Ø, Hvidsten, P., Fritts, D., & Arendt, S. (1998). Vorticity dynamics in a breaking internal gravity wave. Part 1. Initial instability evolution. *Journal of Fluid Mechanics*, 367, 27–46. doi:10.1017/S0022112098001645

- Aumann, H. H., Chahine, M. T., Gautier C., Goldberg, M. D., Kalnay E., McMillin, L. M., et al (2003). AIRS/AMSU/HSB on the Aqua mission: Design, science objectives, data products, and processing systems. *IEEE Transactions on Geoscience and Remote Sensing*, 41(2), 253–264.
- Bacmeister, J. T., & Schoeberl, M. R. (1989). Breakdown of Vertically Propagating Two-Dimensional Gravity Waves Forced by Orography. *Journal of the Atmospheric Sciences*, 46, 2109–2134. doi:10.1175/1520-0469(1989)046<2109:BOVPTD>2.0.CO;2
- Becker, E., & Vadas S. L. (2018). Secondary gravity waves in the winter mesosphere: Results from a high-resolution global circulation model. *Journal of Geophysical Research: Atmospheres*, 123. doi:10.1002/2017JD027460
- Becker, E., & Vadas S. L. (2020). Explicit global simulation of gravity waves in the thermosphere, submitted to *Journal of Geophysical Research: Space Physics*.
- Bossert, K., Fritts, D. C., Pautet, P.-D., Williams, B. P., Taylor, M. J., Kaifler, B., et al. (2015). Momentum flux estimates accompanying multiscale gravity waves over Mount Cook, New Zealand, on 13 July 2014 during the DEEPWAVE campaign. *Journal of Geophysical Research: Atmospheres*, 120, 9323–9337. doi:10.1002/2015JD023197
- Butchart, N., Cionni, I., Eyring, V., Shepherd, T. G., Waugh, D. W., Akiyoshi, H., et al. (2010). Chemistry–Climate Model Simulations of Twenty-First Century Stratospheric Climate and Circulation Changes. *Journal of Climate*, 23, 5349–5374. doi:10.1175/2010JCLI3404.1
- Chahine, M. T., Pagano, T. S., Aumann, H. H., Atlas, R., Barnett, C., Blaisdell, J., et al. (2006). AIRS: Improving Weather Forecasting and Providing New Data on Greenhouse Gases. *Bulletin of the American Meteorological Society*, 87, 911–926. doi:10.1175/BAMS-87-7-911
- de Wit, R. J., Janches, D., Fritts, D. C., Stockwell, R. G., & Coy, L. (2017). Unexpected climatological behavior of MLT gravity wave momentum flux in the lee of the Southern Andes hot spot. *Geophysical Research Letters*, 44, 1182–1191. doi:10.1002/2016GL072311.
- Dunkerton, T.J., (1984). Inertia–Gravity Waves in the Stratosphere. *Journal of the Atmospheric Sciences*, 41, 3396–3404. doi:10.1175/1520-0469(1984)041<3396:IWITS>2.0.CO;2
- Ern, M., Hoffmann, L., & Preusse, P. (2017). Directional gravity wave momentum fluxes in the stratosphere derived from high-resolution AIRS temperature data. *Geophysical Research Letters*, 44, 475–485. doi:10.1002/2016GL072007
- Fritts, D. C., Isler, J. R., & Andreassen, Ø. (1994). Gravity wave breaking in two and three dimensions: 2. Three-dimensional evolution and instability structure. *Journal of Geophysical Research*, 99(D4), 8109– 8123. doi:10.1029/93JD03436
- Fritts, D. C., Arendt S., & Anderassen, Ø. (1998). Vorticity dynamics in a breaking internal gravity wave. Part 2. Vortex interactions and transition to turbulence. *Journal of Fluid Mechanics*, 367, 47–65. doi:10.1017/S0022112098001633
- Fritts, D. C., & Alexander, M. J. (2003). Gravity wave dynamics and effects in the middle atmosphere. *Reviews of Geophysics*, 41, 1003. doi:10.1029/2001RG000106, 1

- 443 Gelaro, R., McCarty, W., Suárez, M. J., Todling, R., Molod, A., Takacs, L., et al. (2017). The
444 Modern-Era Retrospective Analysis for Research and Applications, Version 2 (MERRA-
445 2). *Journal of Climate*, 30, 5419–5454. doi.org/10.1175/JCLI-D-16-0758.1
- 446 Geller, M. A., & Gong, J. (2010). Gravity wave kinetic, potential, and vertical fluctuation
447 energies as indicators of different frequency gravity waves. *Journal of Geophysical*
448 *Research*, 115, D11111. doi:10.1029/2009JD012266
- 449 Heale, C. J., Bossert, K., Snively, J. B., Fritts, D. C., Pautet, P.-D., & Taylor, M.
450 J. (2017), Numerical modeling of a multiscale gravity wave event and its airglow
451 signatures over Mount Cook, New Zealand, during the DEEPWAVE campaign, *Journal*
452 *of Geophysical Research: Atmospheres*, 122, 846–860. doi:10.1002/2016JD025700
- 453 Heale, C. J., Bossert, K., Vadas, S. L., Hoffmann, L., Dörnbrack, A., Stober, G., J. B. Snively, &
454 C. Jacobi (2020). Secondary gravity waves generated by breaking mountain waves over
455 Europe. *Journal of Geophysical Research: Atmospheres*, 125, e2019JD031662.
456 doi:10.1029/2019JD031662
- 457 Hoffmann, L., Xue, X., & Alexander, M. J. (2013). A global view of stratospheric gravity wave
458 hotspots located with Atmospheric Infrared Sounder observations. *Journal of*
459 *Geophysical Research: Atmospheres*, 118, 416– 434. doi:10.1029/2012JD018658
- 460 Hoffmann, L., Alexander, M. J., Clerbaux, C., Grimsdell, A. W., Meyer, C. I., Rößler, T., &
461 Tournier, B., (2014). Intercomparison of stratospheric gravity wave observations with
462 AIRS and IASI. *Atmospheric Measurement Techniques*, 7, 4517–4537.
463 doi.org/10.5194/amt-7-4517-2014
- 464 Hoffmann, L., Spang, R., Orr, A., Alexander, M. J., Holt, L. A., & Stein, O., (2017). A decadal
465 satellite record of gravity wave activity in the lower stratosphere to study polar
466 stratospheric cloud formation. *Atmospheric Chemistry and Physics*, 17, 2901–2920.
467 doi:10.5194/acp-17-2901-2017
- 468 Kogure, M., Nakamura, T., Ejiri, M. K., Nishiyama, T., Tomikawa, Y., & Tsutsumi,
469 M. (2018). Effects of horizontal wind structure on a gravity wave event in the middle
470 atmosphere over Syowa (69°S, 40°E), the Antarctic. *Geophysical Research*
471 *Letters*, 45, 5151–5157. doi:10.1029/2018GL078264
- 472 Kogure, M., Nakamura, T., Ejiri, M. K., Nishiyama, T., Tomikawa, Y., Tsutsumi, M., et al.
473 (2017). Rayleigh/Raman lidar observations of gravity wave activity from 15 to 70 km
474 altitude over Syowa (69°S, 40°E), the Antarctic. *Journal of Geophysical Research:*
475 *Atmospheres*, 122, 7869–7880. doi:10.1002/2016JD026360
- 476 Liu, A. Z., & Swenson, G. R. (2003). A modeling study of O₂ and OH airglow perturbations
477 induced by atmospheric gravity waves. *Journal of Geophysical Research*, 108, 4151.
478 doi:10.1029/2002JD002474, D4
- 479 Liu, X., Yue, J., Xu, J., Wang, L., Yuan, W., Russell, J. M., & Hervig, M. E. (2014). Gravity
480 wave variations in the polar stratosphere and mesosphere from SOFIE/AIM temperature
481 observations. *Journal of Geophysical Research: Atmospheres*, 119, 7368–7381.
482 doi:10.1002/2013JD021439
- 483 Lu, X., Chu, X., Fong, W., Chen, C., Yu, Z., Roberts, B. R., & McDonald, A. J. (2015). Vertical
484 evolution of potential energy density and vertical wave number spectrum of Antarctic

- gravity waves from 35 to 105 km at McMurdo (77.8°S, 166.7°E). *Journal of Geophysical Research: Atmospheres*, 120, 2719–2737. doi:10.1002/2014JD022751
- Liu, X., Xu, J., Yue, J., Vadas, S. L., & Becker, E. (2019). Orographic primary and secondary gravity waves in the middle atmosphere from 16-year SABER observations. *Geophysical Research Letters*, 46, 4512–4522. doi:10.1029/2019GL082256
- Marks, C. J., & Eckermann, S.D. (1995). A Three-Dimensional Nonhydrostatic Ray-Tracing Model for Gravity Waves: Formulation and Preliminary Results for the Middle Atmosphere. *Journal of the Atmospheric Sciences*, **52**, 1959–1984. doi:10.1175/1520-0469(1995)052<1959:ATDNRT>2.0.CO;2
- Miller D. S., William C. S., Jia Y., Steven M. S., Alexander, M. J., Lars H., et al. (2015). Upper atmospheric gravity wave details revealed in nightglow satellite imagery. *Proceedings of the National Academy of Sciences* 112 (49) E6728-E6735. doi: 10.1073/pnas.1508084112
- Nappo, C. J. (2002), *An Introduction to Atmospheric Gravity Waves*. Academic Press, 260.
- Preusse, P., Eckermann, S. D., Ern, M., Oberheide, J., Picard, R. H., Roble, R. G., et al. (2009). Global ray tracing simulations of the SABER gravity wave climatology. *Journal of Geophysical Research*, 114, D08126. doi:10.1029/2008JD011214
- Sato, K., Tateno, S., Watanabe, S., & Kawatani, Y. (2012). Gravity Wave Characteristics in the Southern Hemisphere Revealed by a High-Resolution Middle-Atmosphere General Circulation Model. *Journal of the Atmospheric Sciences*, 69, 1378–1396. doi:10.1175/JAS-D-11-0101.1
- Sato, K., & Yoshiki, M. (2008). Gravity Wave Generation around the Polar Vortex in the Stratosphere Revealed by 3-Hourly Radiosonde Observations at Syowa Station. *Journal of the Atmospheric Sciences*, 65, 3719–3735. doi:10.1175/2008JAS2539.1
- Smith, S., Baumgardner, J., & Mendillo, M. (2009). Evidence of mesospheric gravity-waves generated by orographic forcing in the troposphere. *Geophysical Research Letters*, 36, L08807. doi:10.1029/2008GL036936
- Taylor, M. J., & Hapgood, M. A. (1988), Identification of a thunderstorm as a source of short period gravity waves in the upper atmospheric nightglow emissions, *Planetary and space science*, 36(10), 975–985. doi:10.1016/0032-0633(88)90035-9
- Tomikawa, Y. (2015). Gravity wave transmission diagram. *Ann. Geophys.*, 33, 1479–1484. doi.org/10.5194/angeo-33-1479-2015
- Trinh, Q. T., M. Ern, E. Doornbos, P. Preusse, & M. Riese (2018). Satellite observations of middle atmosphere-thermosphere vertical coupling by gravity waves. *Annals of Geophysics*, 36, 425–444. doi:10.5194/angeo-36-425-2018
- Vadas, S. L., Fritts, D. C., & Alexander M. J. (2003). Mechanism for the Generation of Secondary Waves in Wave Breaking Regions. *Journal of the Atmospheric Sciences*, 60, 194–214. doi:10.1175/1520-0469(2003)060<0194:MFTGOS>2.0.CO;2
- Vadas, S. L., Jia Y., Joe S., Pete S., & Alan L., (2009). A model study of the effects of winds on concentric rings of gravity waves from a convective plume near Fort Collins on 11 May 2004. *Journal of Geophysical Research*, 114, D06103. doi:10.1029/2008JD010753

- 525 Vadas, S. L., Yue J., & Nakamura T., (2012). Mesospheric concentric gravity waves generated
526 by multiple convection storms over the North America Great Plain. *Journal of*
527 *Geophysical Research*, 117, D7. doi:10.1029/2011JD017025
- 528 Vadas, S. L., & Becker, E.(2018). Numerical modeling of the excitation, propagation, and
529 dissipation of primary and secondary gravity waves during wintertime at McMurdo
530 Station in the Antarctic. *Journal of Geophysical Research: Atmospheres*, 123, 9326–
531 9369. doi:10.1029/2017JD027974
- 532 Vadas, S. L., Zhao, J., Chu, X., & Becker E., (2018). The excitation of secondary gravity
533 waves from local body forces: Theory and observation. *Journal of Geophysical*
534 *Research: Atmospheres*, 123, 9296–9325. doi:10.1029/2017JD027970
- 535 Vadas, S. L., & Becker, E. (2019). Numerical modeling of the generation of tertiary gravity
536 waves in the mesosphere and thermosphere during strong mountain wave events over the
537 Southern Andes. *Journal of Geophysical Research: Space Physics*, 124, 7687–
538 7718. doi:10.1029/2019JA026694
- 539 Vadas, S. L., Xu, S., Yue, J., Bossert, K., Becker, E., & Baumgarten, G., (2019). Characteristics
540 of the Quiet-time Hotspot Gravity Waves Observed by GOCE over the Southern Andes
541 on 5 July 2010. *Journal of Geophysical Research: Space Physics*, 124, 7034–7061.
542 doi.org/10.1029/2019JA026693
- 543 Vargas, F., Swenson, G., Liu, A., & Pautet, D. (2016). Evidence of the excitation of a ring-like
544 gravity wave in the mesosphere over the Andes Lidar Observatory. *Journal of*
545 *Geophysical Research: Atmospheres*, 121, 8896–8912. doi:10.1002/2016JD024799
- 546 Wu, D. L., & Eckermann, S. D. (2008). Global Gravity Wave Variances from Aura MLS:
547 Characteristics and Interpretation. *Journal of the Atmospheric Sciences*, 65, 3695–3718.
548 doi.org/10.1175/2008JAS2489.1

Figure 1.

Figures 1. (a) and (b) show brightness temperature perturbations with GWs at altitudes of ~23 and ~40 km in 18:32-18:42 on 24 July 2017, respectively. (c) and (d) show the same as a and b, respectively, but in 05:43-05:54 on 25 July 2017. (e) and (f) show wind at an altitude of 2 km at 12 UT on 24 July and 0 UT on 25 July, respectively.

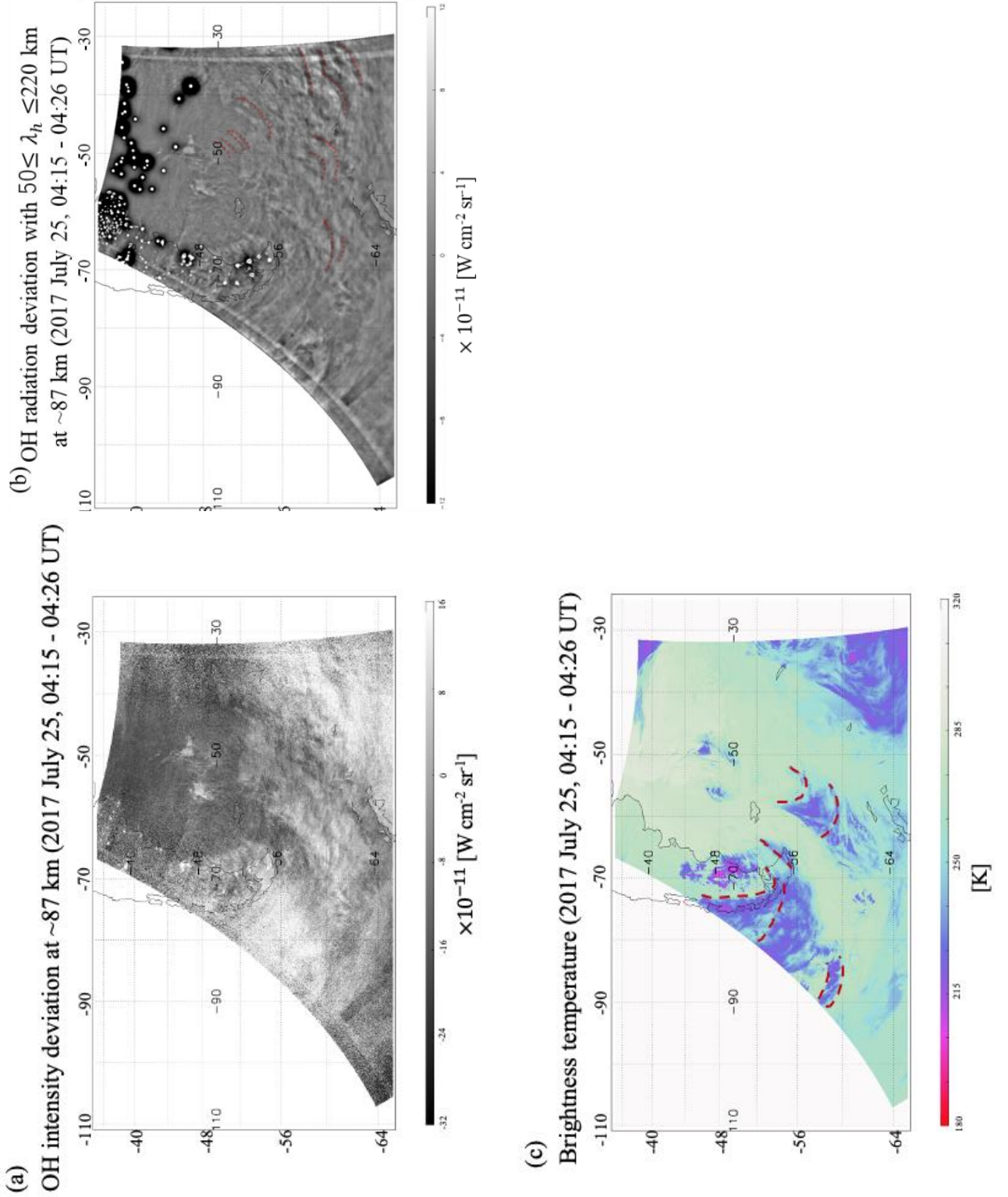


Figure 2. (a) An OH intensity deviation at an altitude of ~ 87 km in 04:15-04:26 on 25 July 2017. (b) The same as (a), but the deviation is applied with a bandpass filter. (c) shows brightness temperatures of clouds at $9.8\text{-}11.8\ \mu\text{m}$.

Figure 3.

OH radiation deviation with $50 \leq \lambda_h \leq 220$ km
at ~ 87 km (2017 July 25, 04:15 - 04:26 UT)

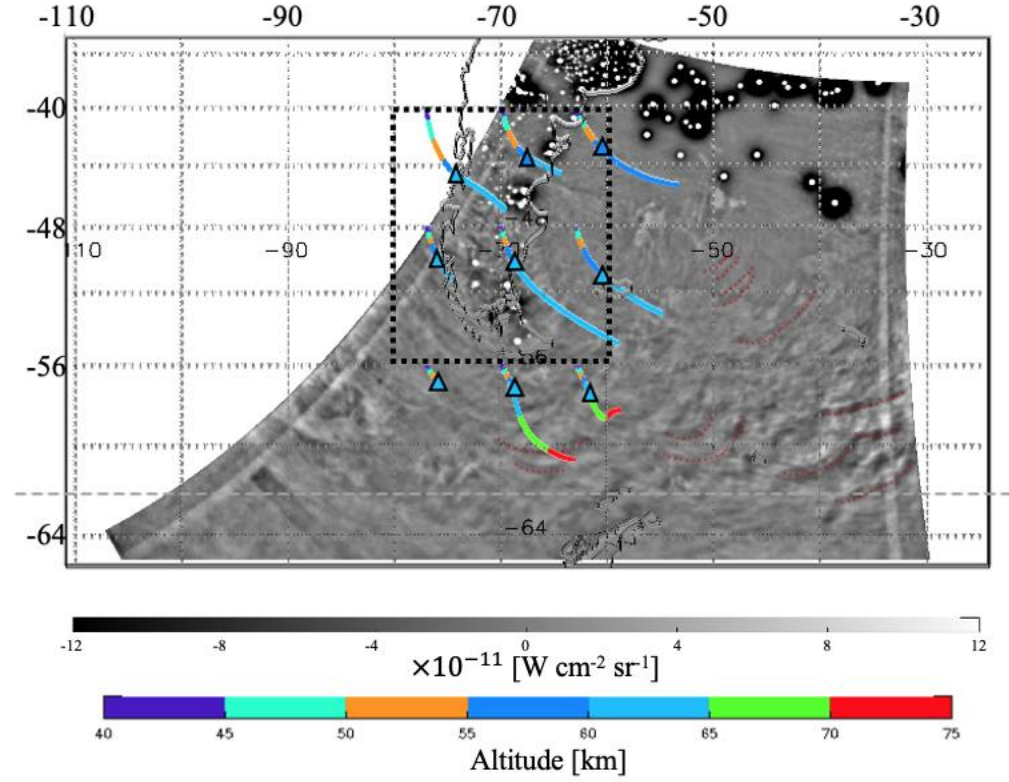


Figure 3. The ray tracing results are superimposed in Figure 2b. These colors indicate the altitude of each mountain wave. The squares indicate the beginning point of a shear instability.

567
568
569
570